nature communications

Article

https://doi.org/10.1038/s41467-025-66063-6

Enhanced tunable X-rays from bulk crystals driven by table-top free electron energies

Received: 12 February 2025

Accepted: 28 October 2025

Published online: 11 December 2025

Check for updates

Qingwei Zhai[1,4], Nikhil Pramanik[1,4], Ruihuan Duan[2,4], Sunchao Huang[1,4], Zheng Liu[1,2,3] & Liang Jie Wong[1]

Free-electron-driven crystalline materials have emerged as a promising platform for tunable, table-top X-ray generation in industrial, medical imaging applications, and fundamental research. It is commonly believed, however, that the use of bulk crystals is not feasible under the weakly relativistic energies necessitated by table-top electron sources. This belief is fueled by the perception that electron scattering inside bulk crystals produces substantial bremsstrahlung background which overwhelms the tunable, narrowband X-ray peaks. In this study, we overturn this belief by introducing a parameter that distinguishes a regime where tunable X-rays substantially dominate bremsstrahlung in bulk materials. We show that this regime is most readily accessible with van der Waals crystals, revealing an unprecedented property of van der Waals crystals in the X-ray regime. We experimentally demonstrate a tenfold intensity enhancement through the use of bulk van der Waals crystals, in good agreement with our theoretical predictions. The use of bulk crystals is also advantageous in requiring less labor-intensive material preparation and being less vulnerable to damage compared to thin films. Our findings pave the way to more efficient and more accessible table-top, tunable, narrowband X-ray sources for safer and more sustainable X-ray imaging in industries including semiconductors and healthcare.

Van der Waals (vdW) materials consist of two-dimensional (2D) atomic planes held together by strong intralayer covalent bonds and weak interlayer vdW forces. Since the first isolation of graphene using adhesive tape in 2004[1], vdW materials have garnered significant research attention due to their intriguing properties and novel phenomena, including the anomalous quantum Hall effect[2], massless Dirac particles[3,4], superconductivity[5], ultrahigh carrier mobility[6,7], ferromagnetism[8,9], strongly bound exciton states[10,11], heterostructures[12,13] and strong spin-orbit coupling[14]. In particular, free-electron-driven vdW crystals have emerged as a promising table-top platform for generating tunable X-rays. Such a platform marries the compactness of conventional X-ray tubes with advantages like tunability of larger, less accessible X-ray facilities, ushering in advanced X-ray imaging modalities on a compact scale for applications including semiconductor failure analysis, medical imaging[15–19], security and fundamental research[20–22].

Free-electron-based light sources have been studied across various platforms[23], including plasmonic single-atom layers[24], metasurfaces[25–27], metamaterials[28], nanostructures[29–32], vdW materials[33] and other mechanisms[34–40], spanning a broad spectral range from terahertz radiation to X-rays[41–45]. Among these, the use of free-electron-driven vdW crystals as a platform for tunable X-ray generation has distinguished itself through features including continuous, real-time photon energy tunability[46,47], multicolor X-ray generation[48],

[1]School of Electrical and Electronic Engineering, Nanyang Technological University, 50 Nanyang Avenue, Singapore, Singapore. [2]School of Materials Science and Engineering, Nanyang Technological University, 50 Nanyang Avenue, Singapore, Singapore. [3]Institute for Functional Intelligent Material, National University of Singapore, 21 Lower Kent Ridge Road, Singapore, Singapore. [4]These authors contributed equally: Qingwei Zhai, Nikhil Pramanik, Ruihuan Duan, and Sunchao Huang. e-mail: liangjie.wong@ntu.edu.sg

water-window X-ray production[49], X-ray caustics[50], quantum recoil[51–53], radiation shaping[54] and heterostructure-enabled X-ray focusing[55]. Free-electron-driven vdW crystals overcome the challenge of current commercial X-ray sources in achieving compactness and photon energy tunability simultaneously[46,48,49]. Conventional X-ray tubes are compact but produce high-intensity characteristic peaks only at fixed photon energies determined by material composition, thus lacking continuous, real-time photon energy tunability. On the other hand, tunable X-ray sources such as synchrotrons and X-ray free-electron lasers[56–60] feature a high degree of tunability but require significant space and high energy consumption[61], making them less accessible for laboratory-scale applications.

The promise of free-electron-driven vdW crystals as a table-top X-ray platform, however, has been undermined by an implied dependence on thin films. Indeed, all studies of free-electron-driven vdW crystals have been confined to vdW thin films with thicknesses typically below 200 nm[46–49,51], which are relatively challenging to produce due to labor-intensive preparation processes[62]. The resulting X-ray flux is thus fundamentally limited by the restricted crystal thickness. The common notion is that bulk crystals would cause so much electron scattering, which makes bremsstrahlung drown out the tunable X-ray peaks. This notion has restricted observation of tunable X-ray radiation using bulk crystals, such as silicon[63], to highly relativistic electron sources with kinetic energies above 30 MeV[64–67] or even hundreds of MeV[68–76]. The use of relativistic electrons, however, is an obstacle to the miniaturization of these sources. As such, the combination of table-top free electron energies and bulk crystals has remained unexplored, with a prevailing notion that it would be an unfeasible platform for producing tunable X-ray peaks.

Here, we overturn this notion by showing that the use of free-electron-driven bulk crystals as a platform for producing tunable X-ray peaks is not only feasible but highly advantageous. Specifically, we show that tunable, narrowband X-ray peaks can not only be observed in vdW bulk crystals driven by table-top free electron energies, but even exhibit tenfold intensity enhancement over the use of thin films. Starting from first-principles electromagnetism and electron scattering theory, we derive a parameter that quantitatively defines the regime where tunable X-rays can surpass bremsstrahlung significantly. Compared with conventional bulk crystals, vdW crystals are much more likely to attain large values of this parameter to access said regime, revealing an intriguing and unprecedented property of vdW crystals in the X-ray regime, and explaining the historical inability to observe tunable X-rays in conventional crystalline bulk materials. These findings are most welcome not only as a way to scale up tunable X-ray intensities, but especially in allowing for the use of bulk target materials, which involve less labor-intensive material preparation and are less vulnerable to damage compared to thin films. Our experimental results are in good agreement with the predictions of our theoretical framework – which fully accounts for electron scattering inside the crystal – in both the spectral bandwidth and the absolute intensity of the emitted X-rays. Our findings open up a new avenue in the optimization of tunable X-ray sources based on free-electron-driven crystalline materials, allowing bulk crystals to be employed toward the enhancement of X-ray intensities, leading to reduced costs, greater efficiency and smaller carbon footprint of the resulting X-ray imaging system.

Results

The mechanisms responsible for the generation of tunable, narrowband X-ray peaks from free-electron-driven crystals are parametric X-ray radiation and coherent bremsstrahlung. Parametric X-ray radiation is an atomic-scale version of Smith-Purcell radiation; the emission comes from free electrons passing through or in the vicinity of periodic structures. Parametric X-ray radiation thus arises from the diffraction of the incident electron's Coulomb field by the crystal's periodic atomic structure – acting as a nanometer-scale diffraction grating on the atomic scale. A higher-order radiation mechanism known as coherent bremsstrahlung[63,71,77–83] can sometimes contribute significantly to the tunable X-ray emission as well. Coherent bremsstrahlung is generated by the periodic undulation of incident electrons due to the periodic potential as it traverses the crystal. In our regime of study, the output X-ray photon energies of the two forms of radiation, namely parametric X-ray radiation and coherent bremsstrahlung, are identical and the peak photon energies are given by[47,77]

$$E_p = \hbar \frac{\mathbf{v}\cdot\mathbf{g}}{1-(\mathbf{v}\cdot\hat{\mathbf{n}}/c)},$$

where $\hbar$ is the reduced Planck constant, $\mathbf{v}$ is the electron velocity, $\mathbf{g}$ is the reciprocal lattice vector of a certain plane of the crystal, $\hat{\mathbf{n}}$ is the unit vector along the observation direction, c is the speed of light in vacuum. In our theoretical framework, the formula employed to calculate tunable X-ray intensity is derived by combining the Monte Carlo simulations of electron scattering and Maxwell's equations, given by[46,48,49,51]

$$\frac{d^2N}{d\omega d\Omega} = \frac{1}{N_e}\frac{\alpha\,\omega}{4\pi^2c^2}\sum_{j=1}^{N_e}\sum_{i=1}^{N_{\mathrm{coll}}^{j}}\left|\int_0^{t_L}\mathbf{v}_i(t)\cdot\mathbf{E}_{\mathbf{k}s}\left[\mathbf{r}_i(t),\omega\right]e^{-i\omega t}dt\right|^2,$$

where N is the number of emitted photons, ω is the angular frequency of the emitted photon, Ω is the solid angle, N_e is the number of electrons incident on the crystal, α is the fine-structure constant, t_L is the electron interaction time with the crystal of the i^{th} electron trajectory segment, $\mathbf{v}_i(t)$ is the velocity of the i^{th} electron trajectory segment of the j^{th} electron at time t, $\mathbf{E}_{\mathbf{k}s}$ represents the eigenmode of the crystal, which is a function of position of the electron $\mathbf{r}_i(t)$ and the angular frequency of the emitted photon ω. More details are available in Supplementary Information (SI) Section S1. As electrons travel through a material, the electron scattering with atoms alters both their kinetic energy and traveling direction, which affects the emitted tunable X-ray spectrum. The electron scattering is simulated by using Monte Carlo method in the CASINO software[84–88]. The electron velocity $\mathbf{v}_i$ and position $\mathbf{r}_i$ for each scattered trajectory segment – defined by the electron path between consecutive collisions – are incorporated into Equation (1) and (2) to obtain the resulting tunable X-ray intensity spectrum.

Figure 1a, b illustrate the Monte Carlo simulations of electron scattering in bulk and thin graphite crystals, respectively. In Fig. 1a, a 20 keV electron beam is incident on a bulk graphite crystal. Owing to the long interaction length with the crystal, the electrons gradually lose all their kinetic energy and eventually come to a complete stop. In contrast, Fig. 1b shows electron scattering in a 29 nm-thick graphite thin film, where most electrons pass through the material with minimal energy loss, less than 0.5% and a slight directional deviation of approximately 3°. In bulk materials, the extended interaction lengths – defined as the total distance an electron travels within the crystal while emitting tunable X-rays – enhance electron-crystal interactions, resulting in higher tunable X-ray emission intensity. Figure 1c shows X-ray spectra generated from a 1 mm-thick highly oriented pyrolytic graphite (HOPG) bulk crystal, with electron energies of 17.5, 20, 22.5, and 25 keV, respectively. In our study, a bulk crystal refers to a crystal that is sufficiently thick to prevent all incident electrons from penetrating through it. In this case, further increasing the crystal's thickness does not affect the tunable X-ray spectrum. Figure 1d presents the X-ray spectra from a 29 nm-thick graphite thin film, measured under the same electron energies as in Fig. 1c. Figure 1c, d reveal a tenfold intensity enhancement with bulk vdW crystals. This finding aligns well with our theoretical predictions, confirming not only that tunable X-ray peaks from bulk crystals are well observable over the bremsstrahlung but also that bulk crystals are more effective than thin films for tunable X-ray generation.

https://doi.org/10.1038/s41467-025-66063-6

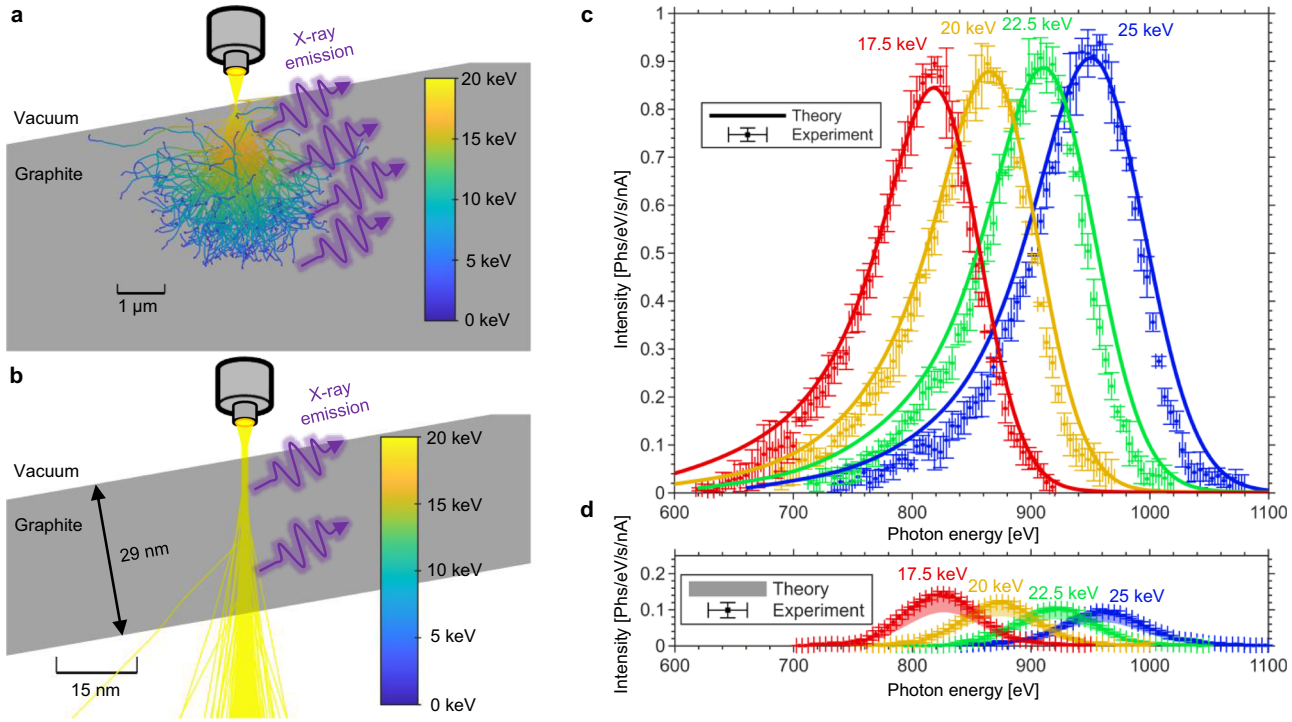

Fig. 1 | Dominance of tunable, narrowband X-rays over bremsstrahlung in bulk van der Waals (vdW) crystals, producing substantial enhancements in X-ray intensity compared to thin films. a Monte Carlo simulation of 20 keV electrons incident on a 1 mm-thick bulk graphite crystal tilted at 10°. The gray region represents the graphite crystal, while the white area depicts free space. Electrons are emitted above the graphite crystal with an initial kinetic energy of 20 keV. The colored trajectories within both the gray (graphite) and white (free space) regions depict electron scattering paths, with colors indicating the corresponding electron kinetic energies. **b** Illustration of a similar scenario with a 29 nm-thick graphite thin film. **c** Tunable X-ray emission from a 1 mm-thick highly oriented pyrolytic graphite (HOPG) bulk crystal, measured under electron energies of 17.5, 20, 22.5, and 25 keV. Solid dots with error bars represent experimental data, while theoretical predictions are shown as solid lines. **d** Tunable X-ray emission from a 29 nm-thick graphite thin film. Solid dots with error bars represent experimental data, translucent bands indicate variations in theoretical predictions due to uncertainties in the thin film thickness under experimental conditions. The definition of the error bars is provided in the Supplementary Information (SI) Section S3. All spectra correspond to a solid angle of 0.066 steradians, which is in accordance with experimental conditions.

Experimental attempts to measure tunable X-ray radiation using bulk crystals and table-top electron sources remain unexplored due to the prevailing notion that relatively high electron scattering in bulk crystals would obscure tunable X-ray peaks beneath the bremsstrahlung background[63]. As we show in Fig. 2a, a regime exists where tunable X-ray peaks substantially dominate bremsstrahlung even in bulk materials. Each point in the figure corresponds to simulation results for different materials (including vdW and conventional materials), crystal planes, and electron energies. The color scale indicates the ratio of tunable X-ray to bremsstrahlung flux within a 10 eV bandwidth around the tunable X-ray peak energy: red denotes ratios $\gtrsim 1$ (tunable X-ray dominates), blue denotes ratios $\lesssim 1$ (bremsstrahlung dominates), and white denotes ratios ≈ 1. The dotted purple line marks the boundary where the two fluxes are approximately equal. This boundary was obtained through numerical fitting from the data in the figure. Above this boundary lies the regime in which tunable X-ray emission tends to dominate, while below this boundary, bremsstrahlung tends to dominate.

As detailed in SI Section S14, we use first-principles electromagnetism and electron scattering theory to obtain the following ratio of the tunable X-ray flux Φ_{tunx} to the bremsstrahlung flux Φ_{brem}, for a given free electron mean free path in the material, as

$$\frac{\Phi_{\mathrm{tunx}}}{\Phi_{\mathrm{brem}}} \propto \frac{E_{\mathrm{p}}[\mathrm{eV}]\left|\chi_{\mathbf{g}}\right|^2}{\left(\frac{Z_{\mathrm{eff}}}{E_{\mathrm{p}}[\mathrm{eV}]}\right) \times T_{\mathrm{accum}}}.$$

In Equation (3), the numerator $E_{\mathrm{p}}\left|\chi_{\mathbf{g}}\right|^2$ originates from the tunable X-ray radiation process. $E_{\mathrm{p}}[\mathrm{eV}] \equiv E_{\mathrm{p}}/(1\mathrm{eV})$ is the value of the photon energy normalized to 1 eV, and $\chi_{\mathbf{g}}$ is the electric susceptibility, which depends on both the crystal plane and photon energy. $\chi_{\mathbf{g}}$ quantifies the diffraction strength of the incident electron's Coulomb field by the crystal's periodic lattice. The denominator $\left(Z_{\mathrm{eff}}/E_{\mathrm{p}}\right) \times T_{\mathrm{accum}}$ originates from the bremsstrahlung contribution, where Z_{eff} is the effective atomic number per unit volume and E_{p} is the bremsstrahlung photon energy. The factor $\left(Z_{\mathrm{eff}}/E_{\mathrm{p}}\right)$ reflects the relative strength of the bremsstrahlung cross-section per unit volume. The factor T_{accum} accounts for the electron distribution after scattering inside the crystal, as well as the resulting X-ray self-absorption, which depends on the electron distribution. As we see in Fig. 2a, plotting Eq. (3) against mean free path separates the data points into two relatively distinct regimes for bulk materials: one where tunable X-ray dominates, and one where bremsstrahlung dominates. The trend of larger mean free paths favoring the dominance of tunable X-rays seen in Fig. 2a is not surprising: this trend can also be inferred from Eq. (2), where we see tunable X-ray emission originating from electron trajectories inside the crystal. A longer electron mean free path increases the interaction time t_{L}, leading to stronger tunable X-ray emission.

Figure 2b repeats the simulation points in Fig. 2a, but shows the category of material being used instead of the flux ratio. Note that conventional materials fall within the tunable X-ray-dominated regime only under very limited conditions, whereas a substantial number of

https://doi.org/10.1038/s41467-025-66063-6

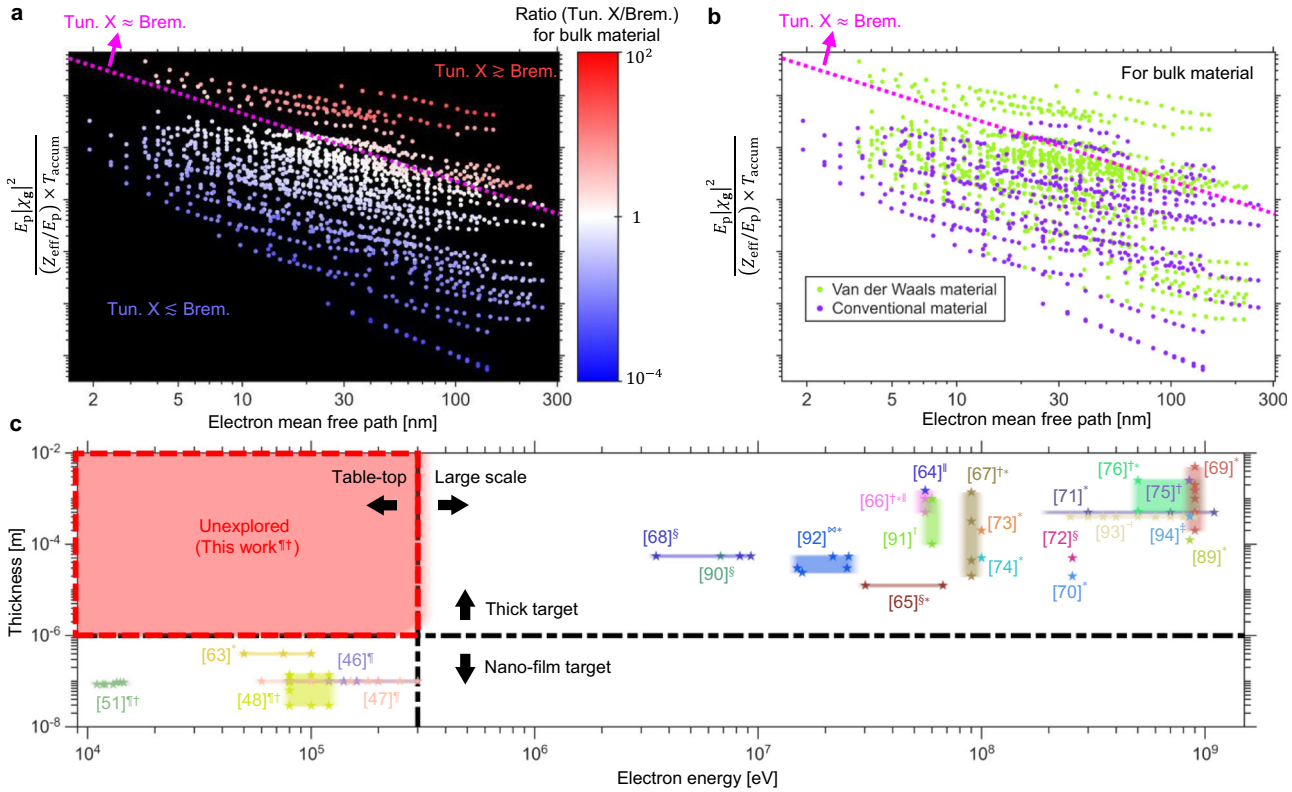

Fig. 2 | Unprecedented regime for free electron-driven X-rays, enabled by the use of van der Waals crystals – where tunable, narrowband X-rays dominate bremsstrahlung even in bulk crystals and at non-relativistic electron energies. **a** Ratio of tunable X-ray flux to bremsstrahlung flux for various conditions, revealing a clear correlation between this ratio and the ordinate expression (Eq. (3)). The points represent simulation results for a broad range of materials, crystal planes, and electron energies. The color scale indicates the ratio of tunable X-ray to bremsstrahlung flux within a 10 eV bandwidth around the tunable X-ray peak energy. Red indicates ratios ≳ 1 (tunable X-ray flux exceeding bremsstrahlung), blue indicates ratios ≲ 1, and white indicates ratios ≈ 1. The boundary where the two fluxes are approximately equal (obtained by numerical fitting of the plotted data) is marked by the dotted purple line. **b** Same plot as in **a**, but with point colors representing different material types as indicated in the legend. **c** Summary of previous free-electron radiation experiments with various material thicknesses and electron kinetic energies. Pentagrams mark the specific material thickness and electron kinetic energy used in each experiment. Shaded regions represent studies encompassing a range of material thicknesses or electron energies. Superscripts next to the references indicate the materials investigated in each study: *silicon, †graphite, §diamond, ‖lithium fluoride, ┬copper, ⋈germanium, ⊣gallium arsenide, ‡tungsten, and ¶ represents various vdW materials including WS_2, MoS_2, WSe_2, $MoSe_2$, h-BN, ZrS_3, $MnPS_3$ and $CrPS_4$.

vdW materials occupy the tunable X-ray dominated regime. Our results reveal an intriguing and unprecedented property of vdW materials in the X-ray regime: namely, their ability to feature a much larger Φ_{tunx}/Φ_{brem} ratio compared to conventional materials, allowing a higher chance of vdW materials emitting tunable X-ray peaks that dominate bremsstrahlung even when the vdW materials are in bulk form and electron scattering of free electrons is significant. The full list of materials and crystal planes used in the simulations is provided in SI Section S14, Supplementary Table 5.

An overview of earlier experimental studies on free-electron radiation using various materials and electron kinetic energies[46–48,51,63–76,89–94] is shown in Fig. 2c. The theoretical regimes of these studies are represented by shaded regions, with pentagrams marking the corresponding material thickness and electron energy for each experiment. Experimental studies in the upper-right corner of Fig. 2c are conducted in the relatively low scattering regime, characterized by large crystal thicknesses and high electron energies. In this regime, electron kinetic energies ranging from a few MeV to over 1 GeV allow electrons to traverse millimeter-scale crystals with minimal energy loss less than 5% and only slight changes in direction, which is less than 10°.

Conversely, recent experimental studies in the lower-left corner of Fig. 2c focus on another relatively low scattering regime, characterized by low crystal thicknesses and low electron energies. Advances in nanoscale thin crystal fabrication have facilitated investigations in this regime using table-top electron sources, such as scanning electron microscopes (SEMs) and transmission electron microscopes (TEMs). Operating at electron energies below 300 keV, these sources enable electrons to traverse nanometer-thick crystals with relatively low electron scattering. Our study reports tunable X-ray emission in the relatively high electron scattering regime, characterized by large crystal thicknesses and low electron energies, as highlighted in the red box in Fig. 2c. Supported by theoretical predictions and experimental data, our work opens up a new avenue for tunable X-ray research under previously unexplored conditions.

Figure 3a illustrates the variation in tunable X-ray intensity with material thickness. Four tunable X-ray spectra collected at different graphite thicknesses under a 25 keV electron energy are shown. As the graphite thickness increases from 29 nm to 1 mm, the tunable X-ray intensity increases significantly, achieving up to a tenfold enhancement experimentally, consistent with our theoretical predictions. The inset in Fig. 3a shows the relationship between tunable X-ray intensity and graphite thickness. Each dot represents the tunable X-ray peak intensity predicted by our theory, which has been validated by experimental data. This relationship can be described by the equation

$$I(l) = I_s(1 - e^{-\frac{l}{L}}),$$

https://doi.org/10.1038/s41467-025-66063-6

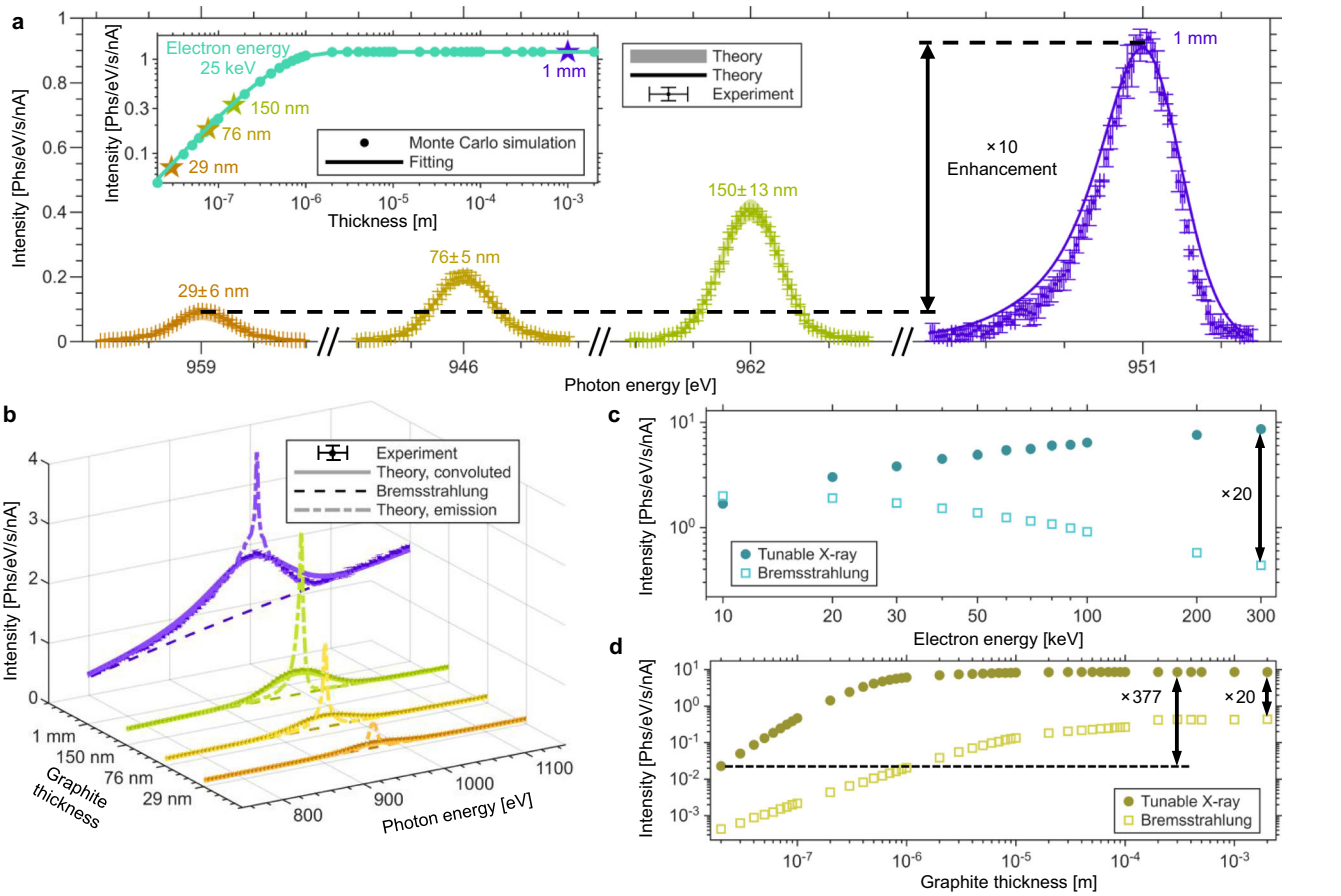

Fig. 3 | Enhancement of tunable, narrowband X-ray peaks by increasing material thickness into the bulk regime. a Demonstrates the enhancement of tunable X-ray intensity from graphite as a function of material thickness. X-ray spectra collected from four distinct graphite samples under a 25 keV electron beam are shown. Solid dots with error bars represent experimental data, while translucent bands and solid lines indicate theoretical predictions. The translucent bands account for intensity variations due to uncertainties in graphite film thickness under experimental conditions. The inset highlights the tunable X-ray intensity trend with increasing thickness at 25 keV for a non-tilted crystal. Solid dots represent simulation results based on the established theory. The solid line represents the fitted curve, while four pentagrams mark the specific thicknesses at which experimental spectra were measured. **b** Compares tunable X-rays with bremsstrahlung background for graphite thin films and bulk graphite under 25 keV electron beams. Solid dots with error bars denote experimental tunable X-ray data, obtained using an energy-dispersive X-ray spectroscopy (EDS) detector alongside bremsstrahlung background. Solid lines depict theoretical tunable X-ray peaks convoluted with the EDS detector resolution, which closely match the experimental data. Dashed lines beneath the tunable X-ray peaks indicate bremsstrahlung background. Sharp dotted lines represent theoretical tunable X-ray peaks calculated without considering the EDS detector resolution. **c** Displays the comparison between tunable X-ray intensity and the bremsstrahlung. Solid round dots represent tunable X-ray intensity values derived from the established theory, validated by experimental results. Hollow squares indicate bremsstrahlung intensity, calculated using the Monte Carlo method[96–100]. **d** Highlights the enhancement of tunable X-ray intensity with increasing material thickness under a 300 keV electron beam. The definition of the error bars is provided in the Supplementary Information (SI) Section S3. All spectra and intensity data correspond to a solid angle of 0.066 steradians, in accordance with experimental conditions.

where I is the tunable X-ray intensity, l is the crystal thickness, I_s is the saturation tunable X-ray intensity, and L is the fitting parameter. The values of I_s and L depend on the material properties and electron energy (details provided in the SI Section S10). Equation (4) accurately characterizes the increase in tunable X-ray intensity with material thickness and its saturation under specific electron energy conditions.

In Fig. 3a, the bremsstrahlung background is subtracted from the experimental data, and the tunable X-ray linewidth is broadened by the energy resolution of the energy-dispersive X-ray spectroscopy (EDS) detector. In Fig. 3b, we address the challenge identified in the previous experimental investigation, where tunable X-rays could not be distinguished from the bremsstrahlung background when using table-top electron sources and crystals thicker than 500 nm[63]. Our measurements (Fig. 3b) from graphite crystals of varying thicknesses clearly reveal tunable X-ray peaks (solid lines) above the bremsstrahlung background (dashed lines), despite broadening effects from the EDS detector. This demonstrates a significant enhancement in tunable X-ray intensity when using vdW materials. In the absence of detector resolution limits, the intrinsic tunable X-ray peaks (dotted lines) exhibit even greater intensity enhancement relative to the bremsstrahlung background. Employing an X-ray detector with higher resolution than EDS would enable direct observation of this stronger enhancement. Further details on the experimental setup limitations and EDS detector resolution are provided in SI Section S4.

Figure 3c compares the intensity of tunable X-ray and bremsstrahlung. Specifically, for a 2 mm-thick graphite sample under electron energies ranging from 10 keV to 300 keV, achievable with table-top electron sources. The tunable X-ray intensity can exceed the bremsstrahlung by up to a factor of 20. Figure 3d shows the dependence of tunable X-ray and bremsstrahlung intensity on graphite thickness at a fixed electron energy of 300 keV. Across all thicknesses, the tunable X-ray intensity consistently surpasses the bremsstrahlung. Notably, compared to emissions from nanometer-thick crystals, bulk graphite crystals exhibit significantly enhanced tunable X-ray intensity, achieving more than a 300-fold increase. Such order-of-magnitude enhancement can be further scaled by increasing the kinetic energy of

https://doi.org/10.1038/s41467-025-66063-6

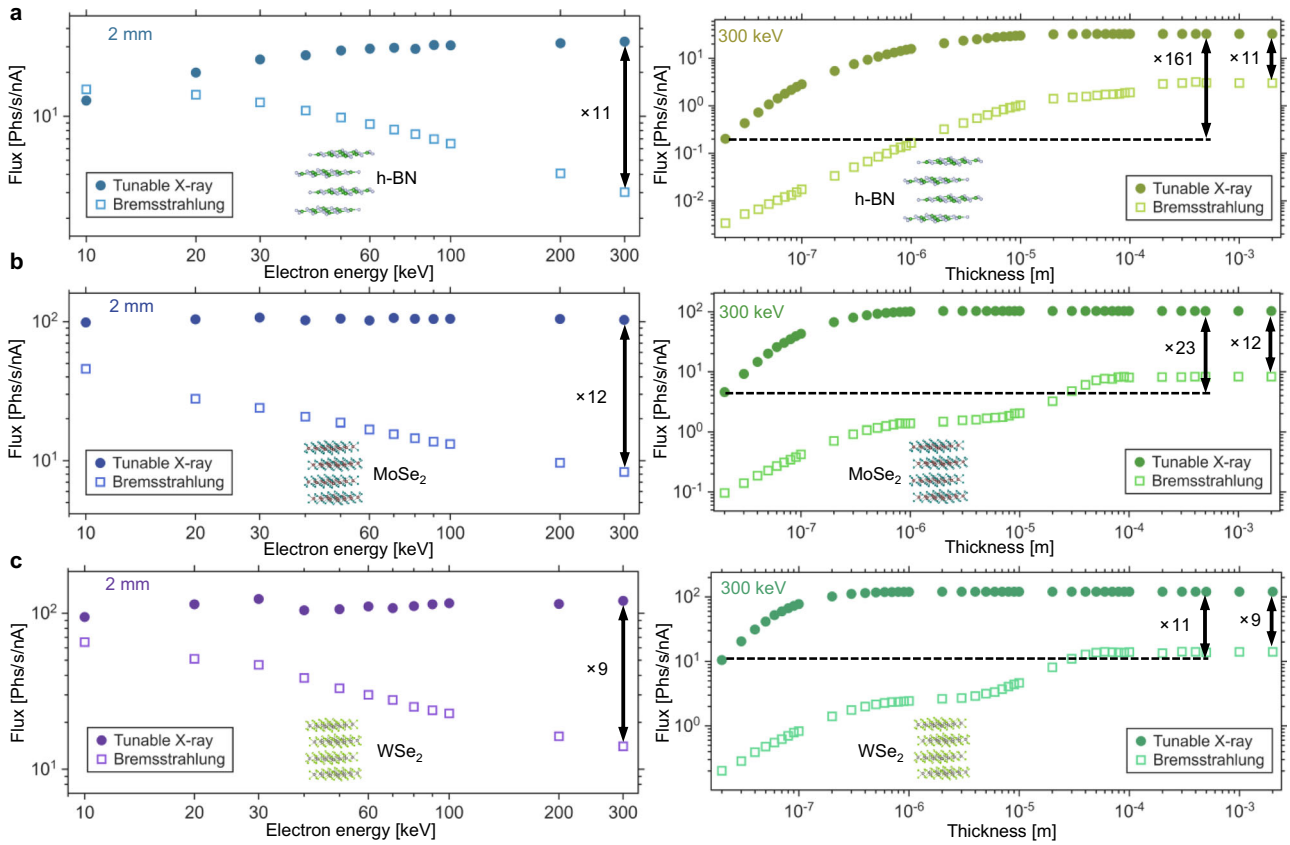

Fig. 4 | Overview of tunable X-ray flux enhancements in different van der Waals (vdW) materials by varying both electron energy and thickness, well into the bulk regime. a Simulated tunable X-ray flux and bremsstrahlung from h-BN. The left panel compares tunable X-ray flux with bremsstrahlung at a fixed material thickness of 2 mm, highlighting the superior tunable X-ray enhancement. The right panel shows the comparison at a fixed electron energy of 300 keV, emphasizing the increased tunable X-ray flux with greater material thickness. Solid dots represent tunable X-ray flux calculated using established theory, while hollow squares denote bremsstrahlung flux obtained via Monte Carlo method[96–100]. **b** Corresponding results for $MoSe_2$ under identical conditions. **c** Corresponding results for WSe_2 under identical conditions. All flux values are calculated for non-tilted crystals by integrating the intensity spectrum within a 10 eV bandwidth around the peak and correspond to a solid angle of 0.066 steradians, in accordance with experimental conditions.

the incident electrons. Nevertheless, even within the table-top electron energy range considered here, the tunable X-ray flux is sufficient to support X-ray applications such as imaging and spectroscopy at practical current densities. The applicability of the tunable X-rays and the maximum current density sustainable by the graphite sample are further detailed in SI Section S11.

The enhancement of tunable X-ray intensity by using bulk materials, as well as the superiority of vdW-based materials in achieving higher tunable X-ray intensity over bremsstrahlung, is not unique to HOPG but extends to a broad range of vdW materials, as demonstrated experimentally in SI Section S7, Supplementary Fig. 5. HOPG was employed here primarily because it is a readily available form of graphite crystal with millimeter-scale thickness. Figure 4 presents simulation results for tunable X-ray and bremsstrahlung background from three different vdW materials: h-BN, $MoSe_2$, and WSe_2. Since photon flux is more commonly referenced in X-ray applications such as X-ray imaging and spectroscopy, the results are expressed in terms of flux rather than intensity. The flux values are calculated by integrating the tunable X-ray and bremsstrahlung intensity spectra within a 10 eV spectral bandwidth centered at the tunable X-ray peak.

The left panels of Fig. 4 illustrate the dependence of tunable X-ray flux on incident electron energy. Specifically, we compare the tunable X-ray flux and bremsstrahlung flux emitted from 2 mm-thick bulk crystals under electron energies ranging from 10 keV to 300 keV, achievable with table-top electron sources. The right panels show the dependence of tunable X-ray flux on material thickness, with the electron energy fixed at 300 keV, where we compare the tunable X-ray and bremsstrahlung flux and examine the tunable X-ray flux emitted from nanometer-thick films versus bulk crystals. At an electron energy of 300 keV and a crystal thickness of 2 mm, tunable X-rays from all three materials exhibit approximately a tenfold enhancement in flux compared to the bremsstrahlung background. Our simulation results reveal that the degree of tunable X-ray enhancement with increasing crystal thickness depends on the material composition. Materials composed of lighter elements, such as h-BN, show greater enhancement due to extended total interaction lengths between electrons and the crystal lattice, and reduced X-ray self-absorption. However, materials composed of heavier elements, such as $MoSe_2$ and WSe_2, exhibit higher absolute tunable X-ray flux values as shown in Fig. 4b, c. A detailed comparison between the tunable X-rays, bremsstrahlung radiation and characteristic X-ray peaks is provided in SI Sections S8 and S9.

Discussion

In this work, we present the theoretical prediction and experimental observation of parametric X-ray radiation in bulk van der Waals (vdW) crystals using table-top free electron source energies. Our findings break the common notion that tunable, narrowband X-ray generation is unfeasible in bulk crystals with table-top free electron sources – on the contrary, we show that the X-ray generation is enhanced. Specifically, we experimentally achieve a tenfold enhancement in the tunable X-ray intensity compared to earlier measurements of free-electron-driven radiation from nanometer-thick films. Importantly, we were also

able to explain the historical inability to observe tunable X-rays in conventional crystalline bulk materials: Starting from first-principles electromagnetism and electron scattering theory, we derived a parameter that quantitatively defines the regime where tunable X-rays can surpass bremsstrahlung significantly. Compared with conventional bulk crystals, vdW crystals are much more likely to attain large values of this parameter to access said regime, revealing an intriguing and unprecedented property of van der Waals crystals in the X-ray regime.

Our experimental results are in good agreement with the results of our theoretical framework, which integrates Monte Carlo simulations of electron scattering within the crystal with Maxwell's equations. We study the dependence of tunable X-ray intensity on crystal thickness and electron energy, showing that tunable narrowband X-ray peaks are significantly enhanced and observable against the bremsstrahlung background over a broad range of material parameters, table-top free electron sources and X-ray photon energies. Our results reveal hitherto untapped advantages of employing bulk vdW crystals in table-top, tunable, narrowband X-ray generation, in addition to the inherent advantages of bulk crystals, which include relative ease of fabrication and resilience against damage as compared to thin films. Our results should pave the way to the design of more compact, efficient and sustainable platforms for table-top, tunable X-ray generation for applications that include semiconductor and biomedical imaging.

Methods

Theory and simulations

The theoretical framework for tunable, narrowband X-ray generation from free-electron-driven crystals is presented in Supplementary Information (SI) Section S1, with detailed explanations and derivations. The geometrical relationship is further illustrated by Supplementary Fig. 1. The Monte Carlo simulations of electron scattering in solids were performed using the CASINO software, with further details provided in SI Section S2.

X-ray measurements

The experimental X-ray spectra containing tunable X-ray peaks were collected using the JEOL 7800 field emission scanning electron microscope (FESEM) equipped with the Oxford UltimMax 170 energy-dispersive X-ray spectroscopy (EDS) detector. Crystalline thin films were mounted on gold transmission electron microscopy grids, while bulk crystals were affixed directly to a nickel scanning electron microscope holder using aluminum stubs and secured with a carbon disc and carbon tapes. The performance of the Oxford UltimMax 170 EDS detector is given in Supplementary Tables 1, 2. More detailed information can be found in SI Section S3.

Sample synthesis and preparation

Graphite nanoflakes were mechanically exfoliated onto silicon substrates coated with a 285 nm SiO_2 layer. The flakes were subsequently transferred onto gold transmission electron microscopy grids via a conventional wet-transfer process. In this procedure, a PMMA layer was spin-coated onto the substrate and baked at 120 °C for 2 min. The underlying SiO_2 was then etched away using a 20 wt% KOH solution, thereby releasing the PMMA film containing the graphite nanoflakes, which was carefully transferred onto the gold transmission electron microscopy grids. To expose the thin graphite layers, the PMMA support was removed by immersion in acetone, followed by thorough drying of the samples on the Au TEM grids.

Sample thickness measurements

The crystal thicknesses were measured using different techniques depending on the thickness range. For crystals thicker than 1 µm, the thickness was directly determined from cross-sectional images obtained via scanning electron microscopy (SEM). For crystals with thicknesses between 300 nm and 1 µm, atomic force microscopy (AFM) was used. For thinner crystals (<300 nm), thickness measurements were conducted using convergent beam electron diffraction (CBED) patterns shown in Supplementary Fig. 3. Crystal thickness values are given in the Supplementary Tables 3a, b. More detailed information can be found in SI Section S6.

Data availability

The raw data that support the plots of this study are openly available in NTU research data repository DR-NTU (Data) at https://doi.org/10.21979/N9/WZAMZO[95].

Code availability

Simulation codes are available from the corresponding authors upon request.

References

1. Novoselov, K. S. et al. Electric field effect in atomically thin carbon films. *Science* **306**, 666–669 (2004).
2. Deng, Y. et al. Quantum anomalous Hall effect in intrinsic magnetic topological insulator $MnBi_2Te_2$. *Science* **367**, 895–900 (2020).
3. Wang, L. et al. One-dimensional electrical contact to a two-dimensional material. *Science* **342**, 614–617 (2013).
4. Shao, Y. et al. Semi-dirac fermions in a topological metal. *Phys. Rev. X* **14**, 041057 (2024).
5. Li, J. et al. Printable two-dimensional superconducting monolayers. *Nat. Mater.* **20**, 181–187 (2021).
6. Banszerus, L. et al. Ultrahigh-mobility graphene devices from chemical vapour deposition on reusable copper. *Sci. Adv.* **1**, e1500222 (2015).
7. Ni, G. X. et al. Ultrafast optical switching of infrared plasmon polaritons in high-mobility graphene. *Nat. Photonics* **10**, 244–247 (2016).
8. Huang, B. et al. Layer-dependent ferromagnetism in a van der Waals crystal down to the monolayer limit. *Nature* **546**, 270–273 (2017).
9. Chapler, B. C. et al. Infrared electrodynamics and ferromagnetism in the topological semiconductors Bi_2Te_3 and Mn-doped Bi_2Te_3. *Phys. Rev. B* **89**, 235308 (2014).
10. Davoodi, F. & Talebi, N. Plasmon–exciton interactions in nanometer-thick gold-WSe_2 multilayer structures: implications for photodetectors, sensors, and light-emitting devices. *ACS Appl. Nano Mater.* **4**, 6067–6074 (2021).
11. Chahshouri, F., Taleb, M., Diekmann, F. K., Rossnagel, K. & Talebi, N. Interaction of excitons with Cherenkov radiation in WSe_2 beyond the non-recoil approximation. *J. Phys. Appl. Phys.* **55**, 145101 (2022).
12. Lin, X. et al. Chiral plasmons with twisted atomic bilayers. *Phys. Rev. Lett.* **125**, 077401 (2020).
13. Yu, R. & Fan, S. Enhanced free-electron–photon interactions at the topological transition in van der waals heterostructures. *Nano Lett.* **25**, 529–536 (2025).
14. Novoselov, K. S., Mishchenko, A., Carvalho, A. & Castro Neto, A. H. 2D materials and van der Waals heterostructures. *Science* **353**, aac9439 (2016).
15. Burchert, J.-P. et al. X-ray phase-contrast tomography of cells manipulated with an optical stretcher. *J. Synchrotron Radiat.* **31**, 923–935 (2024).
16. Reichmann, J. et al. 3D multiscale characterization of the human placenta: Bridging anatomy and histology by X-ray phase-contrast tomography. *PNAS Nexus* **4**, pgae583 (2024).
17. Reichmann, J. et al. 3D imaging of SARS-CoV-2 infected hamster lungs by X-ray phase contrast tomography enables drug testing. *Sci. Rep.* **14**, 12348 (2024).
18. Frost, J. et al. 3d virtual histology reveals pathological alterations of cerebellar granule cells in multiple sclerosis. *Neuroscience* **520**, 18–38 (2023).

19. Reichmann, J. et al. Human lung virtual histology by multi-scale x-ray phase-contrast computed tomography. *Phys. Med. Biol.* **68**, 115014 (2023).
20. de Vos, T. D. C., Postema, J. J., Schaap, B. H., Di Piazza, A. & Luiten, O. J. Production of entangled x rays through nonlinear double Compton scattering. *Phys. Rev. A* **110**, 043702 (2024).
21. Schaap, B. H., Smorenburg, P. W. & Luiten, O. J. Isolated attosecond X-ray pulses from superradiant Thomson scattering by a relativistic chirped electron mirror. *Sci. Rep.* **12**, 19727 (2022).
22. Han, S., Zhao, K. & Chang, Z. Monitoring argon L-shell auger decay using 250-eV attosecond X-ray pulses. *Sensors* **22**, 7513 (2022).
23. Shi, X. et al. Quantum nanophotonics with energetic particles: X-rays and free electrons. *Prog. Quantum Electron.* **102**, 100577 (2025).
24. Wong, L. J., Kaminer, I., Ilic, O., Joannopoulos, J. D. & Soljačić, M. Towards graphene plasmon-based free-electron infrared to X-ray sources. *Nat. Photonics* **10**, 46–52 (2016).
25. Rosolen, G. et al. Metasurface-based multi-harmonic free-electron light source. *Light Sci. Appl.* **7**, 64 (2018).
26. Karnieli, A. et al. Cylindrical metalens for generation and focusing of free-electron radiation. *Nano Lett.* **22**, 5641–5650 (2022).
27. Zhang, X. et al. Hybrid surface waves in twisted anisotropic hetero-metasurfaces. *Phys. Rev. Appl.* **21**, 064034 (2024).
28. Pizzi, A. et al. Graphene metamaterials for intense, tunable, and compact extreme ultraviolet and X-ray sources. *Adv. Sci.* **7**, 1901609 (2020).
29. Rivera, N., Wong, L. J., Joannopoulos, J. D., Soljačić, M. & Kaminer, I. Light emission based on nanophotonic vacuum forces. *Nat. Phys.* **15**, 1284–1289 (2019).
30. Wong, L. W. W. et al. Free-electron crystals for enhanced X-ray radiation. *Light Sci. Appl.* **13**, 29 (2024).
31. Talebi, N. et al. Merging transformation optics with electron-driven photon sources. *Nat. Commun.* **10**, 599 (2019).
32. Gong, Z. et al. Free-electron resonance transition radiation via Brewster randomness. *Proc. Natl Acad. Sci.* **122**, e2413336122 (2025).
33. Taleb, M. et al. Ultrafast phonon-mediated dephasing of color centers in hexagonal boron nitride probed by electron beams. *Nat. Commun.* **16**, 2326 (2025).
34. Chen, R. et al. Free-electron Brewster-transition radiation. *Sci. Adv.* **9**, eadh8098 (2023).
35. Balanov, A., Gorlach, A. & Kaminer, I. Temporal and spatial design of X-ray pulses based on free-electron–crystal interaction. *APL Photonics* **6**, 070803 (2021).
36. Gong, Z. et al. Interfacial Cherenkov radiation from ultralow-energy electrons. *Proc. Natl Acad. Sci.* **120**, e2306601120 (2023).
37. Adiv, Y. et al. Observation of 2D cherenkov radiation. *Phys. Rev. X* **13**, 011002 (2023).
38. Lin, X. et al. Controlling Cherenkov angles with resonance transition radiation. *Nat. Phys.* **14**, 816–821 (2018).
39. Roques-Carmes, C. et al. Free-electron–light interactions in nanophotonics. *Appl. Phys. Rev.* **10**, 011303 (2023).
40. Chen, J. et al. Low-velocity-favored transition radiation. *Phys. Rev. Lett.* **131**, 113002 (2023).
41. Balanov, A., Gorlach, A. & Kaminer, I. Breaking the barriers of electron-driven x-ray radiation in crystals. *APL Photonics* **9**, 076101 (2024).
42. Massuda, A. et al. Smith–purcell radiation from low-energy electrons. *ACS Photonics* **5**, 3513–3518 (2018).
43. Ye, Y. et al. Deep-ultraviolet Smith–Purcell radiation. *Optica* **6**, 592 (2019).
44. Chen, J., Chen, H. & Lin, X. Photonic and plasmonic transition radiation from graphene. *J. Opt.* **23**, 034001 (2021).
45. Taleb, M., Hentschel, M., Rossnagel, K., Giessen, H. & Talebi, N. Phase-locked photon–electron interaction without a laser. *Nat. Phys.* **19**, 869–876 (2023).
46. Huang, S. et al. Enhanced versatility of table-top X-rays from van der waals structures. *Adv. Sci.* **9**, 2105401 (2022).
47. Shentcis, M. et al. Tunable free-electron X-ray radiation from van der Waals materials. *Nat. Photonics* **14**, 686–692 (2020).
48. Huang, S. et al. Multicolor x-rays from free electron–driven van der Waals heterostructures. *Sci. Adv.* **9**, eadj8584 (2023).
49. Pramanik, N. et al. Fundamental scaling laws of water-window X-rays from free-electron-driven van der Waals structures. *Nat. Photonics* **18**, 1203–1211 (2024).
50. Shi, X. et al. Free-electron-driven X-ray caustics from strained van der Waals materials. *Optica* **10**, 292–301 (2023).
51. Huang, S. et al. Quantum recoil in free-electron interactions with atomic lattices. *Nat. Photonics* https://doi.org/10.1038/s41566-022-01132-6 (2023).
52. Talebi, N. Tunable quantum recoil. *Nat. Photonics* **17**, 213–214 (2023).
53. Shi, X., Wong, L. W. W., Huang, S., Wong, L. J. & Kaminer, I. Transverse recoil imprinted on free-electron radiation. *Nat. Commun.* **15**, 7803 (2024).
54. Lin, X. & Chen, H. Shaping free-electron radiation via van der Waals heterostructures. *Light Sci. Appl.* **12**, 187 (2023).
55. Shi, X. et al. Free-electron interactions with van der Waals heterostructures: a source of focused X-ray radiation. *Light Sci. Appl.* **12**, 148 (2023).
56. Carbajo, S. Light by design: emerging frontiers in ultrafast photon sciences and light–matter interactions. *J. Phys. Photonics* **3**, 031001 (2021).
57. Carbajo, S., Fallahi, A., Faure, J. & Wong, L. J. Editorial: lasers in accelerator science and secondary emission light source technology. *Front. Phys.* **7**, 162 (2019).
58. Zhang, H. et al. The Linac Coherent Light Source II photoinjector laser infrastructure. *High. Power Laser Sci. Eng.* **12**, e51 (2024).
59. Lueangaramwong, A., Andonian, G. & Piot, P. Application of transverse-to-longitudinal phase-space-exchanged beam produced from a nano-structure photocathode to a soft x-ray free-electron laser. *Proc. 9th Int Part. Accel. Conf* **IPAC2018**, 3 pages, 15.431 MB (2018).
60. Hermann, B. et al. Laser-driven modulation of electron beams in a dielectric micro-structure for x-ray free-electron lasers. *Sci. Rep.* **9**, 19773 (2019).
61. Brau, C. A., Choi, B.-K., Jarvis, J. D., Lewellen, J. W. & Piot, P. Channeling radiation as a source of hard X-rays with high spectral brilliance. *Synchrotron Radiat. N.* **25**, 20–24 (2012).
62. Choi, S. H. et al. Large-scale synthesis of graphene and other 2D materials towards industrialization. *Nat. Commun.* **13**, 1484 (2022).
63. Baryshevsky, V. G. et al. Coherent bremsstrahlung and parametric X-ray radiation from nonrelativistic electrons in a crystal. *Tech. Phys. Lett.* **32**, 392–395 (2006).
64. Sones, B., Danon, Y. & Block, R. C. X-ray imaging with parametric X-rays (PXR) from a lithium fluoride (LiF) crystal. 9 (2006).
65. Freudenberger, J., Genz, H., Morokhovskyi, V. V., Richter, A. & Sellschop, J. P. F. Parametric X rays observed under bragg condition: boost of intensity by a factor of two. *Phys. Rev. Lett.* **84**, 270–273 (2000).
66. Sones, B., Danon, Y. & Block, R. C. Lithium fluoride (LiF) crystal for parametric X-ray (PXR) production. *Nucl. Instrum. Methods Phys. Res. Sect. B Beam Interact. Mater.* **227**, 22–31 (2005).
67. Fiorito, R. B. et al. Observation of higher-order parametric x-ray spectra in mosaic graphite and single silicon crystals. *Phys. Rev. Lett.* **71**, 704–707 (1993).

68. Freudenberger, J. et al. Parametric X-ray radiation observed in diamond at low electron energies. *Phys. Rev. Lett.* **74**, 2487–2490 (1995).
69. Endo, I. et al. Parametric X radiation from thick crystals. *Phys. Rev. E* **51**, 6305–6308 (1995).
70. Berdnichenko, A. V., Shatokhin, R. A., Takabayashi, Y. & Vnukov, I. E. Observation of parametric X-ray radiation for the asymmetric Laue geometry. *Phys. Lett. A* **409**, 127537 (2021).
71. Asano, S. et al. How intense is parametric X radiation? *Phys. Rev. Lett.* **70**, 3247–3250 (1993).
72. Takabayashi, Y., Korotchenko, K. B., Pivovarov, Y.uL. & Tukhfatullin, T. A. Angular distributions of parametric X-ray radiation from a diamond crystal. *Nucl. Instrum. Methods Phys. Res. Sect. B Beam Interact. Mater.* **402**, 79–82 (2017).
73. Hayakawa, Y. et al. X-ray imaging using a tunable coherent X-ray source based on parametric X-ray radiation. *J. Instrum.* **8**, C08001–C08001 (2013).
74. Takahashi, Y. et al. Parametric X-ray radiation as a novel source for X-ray imaging: PXR for X-ray imaging. *X-Ray Spectrom.* **41**, 210–215 (2012).
75. Chefonov, O. et al. Experimental comparison of parametric X-ray radiation and diffracted bremsstrahlung in a pyrolytic graphite crystal. *Nucl. Instrum. Methods Phys. Res. Sect. B Beam Interact. Mater.* **173**, 18–26 (2001).
76. Bogomazova, E. A. et al. Diffraction of real and virtual photons in a pyrolytic graphite crystal as source of an intensive quasimonochromatic X-ray beam. *Nucl. Instrum. Methods Phys. Res. Sect. B Beam Interact. Mater.* **201**, 276–291 (2003).
77. Feranchuk, I. D., Ulyanenkov, A., Harada, J. & Spence, J. C. H. Parametric x-ray radiation and coherent bremsstrahlung from nonrelativistic electrons in crystals. *Phys. Rev. E* **62**, 4225–4234 (2000).
78. Baryshevskiĭ, V. G., Feranchuk, I. D. & Ulyanenkov, A. P. Parametric X-ray radiation in crystals: theory, experiment, and applications. (Springer, Berlin; New York, 2005).
79. Baryshevsky, V. G. & Feranchuk, I. D. Parametric X-rays from ultrarelativistic electrons in a crystal: theory and possibilities of practical utilization. *J. Phys.* **44**, 913–922 (1983).
80. Reese, G. M., Spence, J. C. H. & Yamamoto, N. Coherent bremsstrahlung from kilovolt electrons in zone axis orientations. *Philos. Mag. A* **49**, 697–716 (1984).
81. Baryshevsky, V. G., Feranchuk, I. D., Grubich, A. O. & Ivashin, A. V. Theoretical interpretation of parametric X-ray spectra. *Nucl. Instrum. Methods Phys. Res. Sect. Accel. Spectrom. Detect. Assoc. Equip.* **249**, 306–319 (1986).
82. Feranchuk, I. D. & Ivashin, A. V. Theoretical investigation of the parametric X-ray features. *J. Phys.* **46**, 1981–1986 (1985).
83. Baryshevsky, V. G. & Feranchuk, I. D. Parametric beam instability of relativistic charged particles in a crystal. *Phys. Lett. A* **102**, 141–144 (1984).
84. Drouin, D. et al. CASINO V2.42—a fast and easy-to-use modeling tool for scanning electron microscopy and microanalysis users. *Scanning* **29**, 92–101 (2007).
85. Demers, H. et al. Three-dimensional electron microscopy simulation with the CASINO Monte Carlo software. *Scanning* **33**, 135–146 (2011).
86. Czyżewski, Z., MacCallum, D. O., Romig, A. & Joy, D. C. Calculations of Mott scattering cross section. *J. Appl. Phys.* **68**, 3066–3072 (1990).
87. Drouin, D., Hovington, P. & Gauvin, R. CASINO: a new monte carlo code in C language for electron beam interactions—part II: tabulated values of the mott cross section. *Scanning* **19**, 20–28 (1997).
88. Joy, D. C. & Luo, S. An empirical stopping power relationship for low-energy electrons. *Scanning* **11**, 176–180 (1989).
89. Brenzinger, K.-H. et al. How narrow is the linewidth of parametric X-ray radiation? *Phys. Rev. Lett.* **79**, 2462–2465 (1997).
90. Freudenberger, J. et al. Experimental determination of the linewidth of parametric X-ray radiation at electron energies below 10 MeV. *Nucl. Instrum. Methods Phys. Res. Sect. B Beam Interact. Mater.* **115**, 408–410 (1996).
91. Sones, B., Danon, Y. & Blain, E. Experiments with relativistic electrons producing tunable X-rays from Cu crystals. *Trans. Am. Nucl. Soc.* **98**, 395–397 (2008).
92. Adejishvili, D. I., Gavrikov, V. B. & Romanov, V. A. On the absolute intensity of parametric X-radiation. *Nucl. Instrum. Methods Phys. Res. Sect. B Beam Interact. Mater.* **152**, 406–408 (1999).
93. Afanasenko, V. P. et al. Detection of parametric X-ray radiation of a GaAs monocrystal. *Phys. Lett. A* **141**, 311–313 (1989).
94. Backe, H. et al. Forward diffracted parametric X radiation from a thick Tungsten single crystal at 855 MeV electron energy. in (ed. Dabagov, S. B.) 66340Z-66340Z–15 https://doi.org/10.1117/12.741924.(2007).
95. Zhai Q. et al. Enhanced tunable X-rays from bulk crystals driven by table-top free electron energies. DR-NTU (Data) https://doi.org/10.21979/N9/WZAMZO (2025).
96. Newbury, D. E. & Ritchie, N. W. M. Energy-dispersive X-ray spectrum simulation with NIST DTSA-II: comparing simulated and measured electron-excited spectra. *Microsc. Microanal.* **28**, 1905–1916 (2022).
97. Newbury, D. E. & Ritchie, N. W. Quantitative electron-excited X-ray microanalysis with low-energy L-shell X-ray peaks measured with energy-dispersive spectrometry. *Microsc. Microanal.* **27**, 1375–1408 (2021).
98. Newbury, D. E. & Ritchie, N. W. M. Performing elemental microanalysis with high accuracy and high precision by scanning electron microscopy/silicon drift detector energy-dispersive X-ray spectrometry (SEM/SDD-EDS). *J. Mater. Sci.* **50**, 493–518 (2015).
99. Ritchie, N. W. M. Spectrum simulation in DTSA-II. *Microsc. Microanal.* **15**, 454–468 (2009).
100. Ritchie, N. W. M., Newbury, D. E. & Davis, J. M. EDS measurements of X-ray intensity at wds precision and accuracy using a silicon drift detector. *Microsc. Microanal.* **18**, 892–904 (2012).

Acknowledgments

We thank L. W. W. Wong, A. Lim, Y. Y. Tay, and D. Ang for helpful discussions. This project is supported by the Ministry of Education (MOE), Singapore, under its Academic Research Fund (AcRF) Tier 1 (RG139/23) and Tier 2 (MOE-T2EP50222-0012) programs. R. D. and Z. L. acknowledge support from the MOE AcRF Tier 3 (MOE2018-T3-1-002) program, and the National Research Foundation Competitive Research Program (NRF-CRP22-2019-0007, NRF-CRP22-2019-0004, NRF-CRP26-2021-0004). We acknowledge the Facility for Analysis, Characterization, Testing and Simulation, Nanyang Technological University, Singapore, for the use of their electron microscopy/X-ray facilities.

Author contributions

Q.Z. performed the experiments and simulations, and drafted the manuscript with the close assistance and guidance of N.P., L.J.W., and S.H.; R.D. and Z.L. fabricated all samples used in this study. L.J.W. conceived the idea and supervised the research.

Competing interests
The authors declare no competing interests.

Additional information
Supplementary information The online version contains supplementary material available at https://doi.org/10.1038/s41467-025-66063-6.

Correspondence and requests for materials should be addressed to Liang Jie Wong.

Peer review information *Nature Communications* thanks Martin Kozák and the other anonymous reviewer(s) for their contribution to the peer review of this work. A peer review file is available.